Nonthermal excitonic condensation near a spin-state transition

Philipp Werner [1] and Yuta Murakami [2]

[1]*Department of Physics, University of Fribourg, 1700 Fribourg, Switzerland*
[2]*Department of Physics, Tokyo Institute of Technology, Meguro, Tokyo 152-8551, Japan*

Recent experiments demonstrate the induction of long-range order in correlated electron systems via external perturbations, which calls for a better understanding of nonthermal ordered states and nonequilibrium symmetry breaking. Here, we reveal a mechanism based on entropy cooling and entropy trapping in a strongly correlated multiorbital system. We consider a two-orbital Hubbard model with Hund coupling and crystal-field splitting and show that in the vicinity of a spin-state transition, crystal-field quenches can induce an excitonic condensation at initial temperatures above the highest ordering temperature in equilibrium. We furthermore identify a dynamical phase transition in the evolution of the order parameter and show that such quenches can result in long-lived nonthermal excitonic condensates which have no analog in the equilibrium phase diagram.

The nonequilibrium control of electronic orders in correlated systems is an intriguing prospect with potentially important technological applications. Several recent experiments suggest that photoexcitation can induce or enhance superconducting [1–4], charge density wave [5], or excitonic [6,7] order. This raises fundamental questions about the physical mechanisms which can trigger and transiently stabilize nonthermal long-range orders. Intensive theoretical efforts are under way to search for new concepts and ideas, with the goal of revealing possible mechanisms in the study of simple but relevant model systems [8–24]. One promising direction is to focus on the entropy and its reshuffling among different degrees of freedom. This entropy cooling idea has been theoretically explored in different contexts [8,14,16,25–27] and successfully employed in cold-atom experiments [28,29]. For example, spin-triplet excitons were suggested as a possible entropy sink in photo-excited fulleride superconductors [14]. This concept is relevant if the subsystem absorbing entropy is decoupled for sufficiently long times, or in an adiabatic scenario if the entropy reshuffling leads to thermalization in a lower temperature state. Important open questions concern nonadiabatic protocols and the possibility of transient ordering associated with thermalization bottlenecks (prethermalization) [30,31].

In order to explore entropic effects on nonequilibrium dynamics and nonthermal order, we consider multiorbital Hubbard systems, which are the generic models for strongly correlated materials. In these systems, the competition between Hund coupling (which favors high-spin states with singly occupied orbitals) and crystal-field splitting (which favors orbital polarization) can lead in equilibrium to spin-state transitions [32], and complex ordering phenomena, including excitonic insulator (EI) phases [33–37]. A spin-state transition is accompanied by a large change of spin entropy, which may be utilized to cool down the system. In this Rapid Communication, we focus on the simplest relevant multiorbital model, the two-orbital Hubbard model, and show that entropy

cooling induced by crystal-field quenches allows us to realize excitonic condensates at initial temperatures above the highest transition temperature. Interestingly, we find transient ordered states controlled by entropy trapping, and a dynamical transition [38–45] in the order parameter dynamics, which separates a thermal-like from a distinctly nonthermal behavior.

The two-orbital Hubbard model describes a local interaction $H_{\text{int}} = \sum_a U n_{a,\uparrow} n_{a,\downarrow} + \sum_\sigma [U' n_{1,\sigma} n_{2,\bar\sigma} + (U' - J) n_{1,\sigma} n_{2,\sigma}] - J(c_{1\downarrow}^\dagger c_{2\uparrow}^\dagger c_{2\downarrow} c_{1\uparrow} + \text{H.c.}) + I(c_{2\uparrow}^\dagger c_{2\downarrow}^\dagger c_{1\uparrow} c_{1\downarrow} + \text{H.c.})$ parametrized by the intraorbital interaction U, Hund coupling J ($U' = U - 2J$), and pair-hopping interaction I, and a crystal-field splitting $H_{\text{cf}} = \Delta_{\text{cf}}(n_1 - n_2)$, where $a = 1, 2$ denotes the orbitals, σ is the spin, $n_{a\sigma} = c_{a\sigma}^\dagger c_{a\sigma}$ indicates the spin- and orbital-dependent density, and $n_a = (n_{a\uparrow} + n_{a\downarrow})$. There is an orbital diagonal nearest-neighbor hopping v and an orbital off-diagonal hopping v'. We treat the lattice model within the dynamical mean-field theory (DMFT) [46] assuming an infinitely connected Bethe lattice. In this case, the hybridization function matrix $\boldsymbol{\Delta}(t, t')$ of the DMFT impurity problem is determined directly by the local Green's function matrix $\mathbf{G}(t, t')$ through $\boldsymbol{\Delta}(t, t') = \mathbf{V}\mathbf{G}(t, t')\mathbf{V}$, where $\mathbf{G}(t, t') = -i\langle T_C \psi(t)\psi^\dagger(t')\rangle$ [47] with $\psi^\dagger = (c_{1\uparrow}^\dagger, c_{2\uparrow}^\dagger, c_{1\downarrow}^\dagger, c_{2\downarrow}^\dagger)$, and $\mathbf{V} = \text{diag}(\mathbf{v}, \mathbf{v})$. Here, $\mathbf{v}$ denotes a 2×2 matrix with $(v, -v)$ on the diagonal and v' on the off diagonal. In the following, we set $I = J$ and $v' = v$, and use $v = 1$ as the unit of energy. The DMFT impurity problem is solved by the noncrossing approximation (NCA) [48,49].

We first discuss the equilibrium phase diagram of this model at half-filling. The competition between the Hund coupling and crystal-field splitting leads, in the strongly correlated regime and at low temperatures, to a transition between a high-spin Mott insulator (HI) with approximately one electron per orbital and a low-spin insulator (LI) with almost two electrons in the lower orbital [32]. Kunes and coworkers showed that the region in the vicinity of the spin-state transition (or crossover) is unstable to staggered high-spin/low-spin
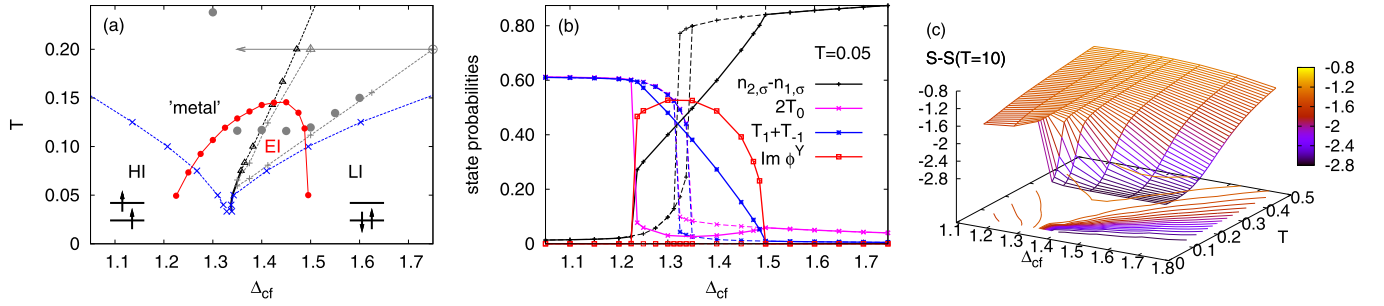
FIG. 1. (a) Phase diagram of the half-filled model for $U = 6$ and $J = 1$. The black lines show the high-spin/low-spin transition (solid) or crossover (dashed), while blue dashed lines indicate the insulator-metal crossover defined by $\frac{1}{T} G_{a\sigma}(\frac{1}{2T}) = 0.033$. Red dots indicate the EI phase. (b) Orbital polarization (black), relevant local states (pink and blue, see text for the definition), and EI OP (red) as a function of crystal-field splitting at $T = 0.05$. The first-order transition with hysteresis in the absence of symmetry breaking is shown by the dashed lines. (c) Entropy per site in the symmetric phase, relative to the value at $T = 10$. The bottom plane shows the constant entropy contours.

or excitonic order [34,35], i.e., a spontaneous hybridization of high-spin and low-spin states. Following Ref. [35], we define the spin-triplet excitonic order parameters (OPs) as

$$\phi^\lambda = \sum_{\sigma\sigma'} \langle c_{1\sigma}^\dagger c_{2\sigma'} \rangle \sigma_{\sigma\sigma'}^\lambda, \qquad (1)$$

where $\sigma_{\sigma\sigma'}^\lambda$ denotes the Pauli matrix for $\lambda = X, Y, Z$ [50].

The phase diagram in the space of crystal-field splitting Δ_{cf} and temperature T is shown in Fig. 1(a) for $U = 6$ and $J = 1$. Let us first discuss the transitions and crossovers in the absence of spontaneous symmetry breaking (blue and black lines). In the atomic limit, the level crossing associated with the high-spin/low-spin transition occurs at $\Delta_{cf} = \sqrt{2}J$ [32]. In the DMFT+NCA solution, it is shifted to slightly lower values (≈ 1.34 at low T). The solid black line corresponds to a first-order phase transition, while the dashed line at $T \gtrsim 0.075$ indicates a high-spin/low-spin crossover.

The low-temperature region around the spin-state transition is unstable to EI order [34,35]. ϕ^X, ϕ^Y, and ϕ^Z are equivalent by symmetry, and we consider EI with nonzero ϕ^Y and zero $\phi^{X,Z}$, without loss of generality. Since we apply a small seed field in the imaginary ϕ^Y direction, the EI phase (indicated by the red line in the phase diagram) corresponds to a purely imaginary ϕ^Y (or real $\langle c_{1\uparrow}^\dagger c_{2\downarrow} - c_{1\downarrow}^\dagger c_{2\uparrow} \rangle$). In Fig. 1(b), we plot the weight of the relevant local states and the OP for fixed $T = 0.05$ against Δ_{cf}. Dashed lines show the results without symmetry breaking, with a small hysteresis region around the first-order transition, and full lines show those in the presence of excitonic order. The black line indicates the orbital polarization, $n_{1,\sigma} - n_{2,\sigma}$, the pink line marked with "$2T_0$" is twice the combined weight of the $|\uparrow, \downarrow\rangle$ $(= \hat{c}_{1\uparrow}^\dagger \hat{c}_{2\downarrow}^\dagger |\text{vac}\rangle)$ and $|\downarrow, \uparrow\rangle$ states, and the blue line marked with "$T_1 + T_{-1}$" indicates the combined weight of the $|\uparrow, \uparrow\rangle$ and $|\downarrow, \downarrow\rangle$ states.

Since the LI is spin singlet and the HI spin triplet, we expect a substantial change in the spin entropy near the high-spin/low-spin transition or crossover. The entropy can be obtained by integrating C_V/T (with $C_V = dE_{tot}/dT$ the specific heat) from high temperatures: $S(T) = S_\infty - \int_T^\infty C_V(T')/T' dT'$. Figure 1(c) plots the change in the entropy per site for the paramagnetic normal states, relative to the value at $T = 10$. At $T \lesssim 0.075$, we see the appearance of a discontinuity associated with the spin-state transition, where the entropy per site changes by approximately $\ln(4)$. On the

bottom plane, we also show the isentropy contours, which on the low-spin side of the spin-state crossover converge toward the low-temperature phase transition line. Two of these contours are indicated as dashed gray lines in Fig. 1(a).

To explore the nonequilibrium dynamics in the vicinity of the spin-state transition, we start at $\Delta_{cf} = 1.75$ and $T = 0.2$ [empty gray dot in Fig. 1(a)], which is above the maximum T_c of about 0.145, and suddenly reduce Δ_{cf} (quench). A small constant seed field of $10^{-3}(c_{1\uparrow}^\dagger c_{2\downarrow} - c_{1\downarrow}^\dagger c_{2\uparrow} + \text{H.c.})$ is applied to allow for EI symmetry breaking. If instead of a quench, we would perform a slow adiabatic ramp, the system would stay in equilibrium, follow the gray dashed line, and enter the symmetry-broken phase with $\text{Im}\phi^Y \neq 0$ around $\Delta_{cf} \approx 1.48$. After a quench, however, it is only possible to determine the point in the phase diagram which will be reached after thermalization [see full gray dots in Fig. 1(a)], using E_{tot} which is conserved for time $t > 0$ [41]. On the other hand, the trajectory from the initial to this final state involves nonthermal states.

Figure 2(a) shows the time evolution of $\text{Re}\phi^Y$ and $\text{Im}\phi^Y$ after a quench to $\Delta_{cf} = 1.4$ (blue lines) and 1.3 (black lines), while the arrows indicate the values of $\text{Im}\phi^Y$ that will be reached after thermalization. After the quench to $\Delta_{cf} = 1.4$, the system is expected to thermalize in the EI, at a temperature substantially below the initial $T = 0.2$, which is the result of entropy cooling, i.e., the electronic system cools down because the entropy in the spin sector increases after the quench. This is qualitatively similar to the adiabatic case.

More surprising is the result after the quench to $\Delta_{cf} = 1.3$, where the energy injected by the quench dominates the cooling effect and results in a thermalization at $T = 0.238$, far above the equilibrium EI phase [see gray dot in Fig. 1(a)]. Nevertheless, the complex OP grows to values comparable to the previous simulation, which shows that there occurs a symmetry breaking to a nonthermal EI with $|\phi^Y| > 0$. While this transient electronic order will melt at sufficiently long times, the DMFT results show that it lives much longer than the longest simulation time, which for typical bandwidths corresponds to $O(100)$ fs. As shown in the Supplemental Material (SM) [51], no EI phase is induced in quenches from high-spin states due to the lack of entropy cooling.

It is instructive to plot the traces of the complex OPs for different values of the postquench Δ_{cf}; see Fig. 2(b). In the
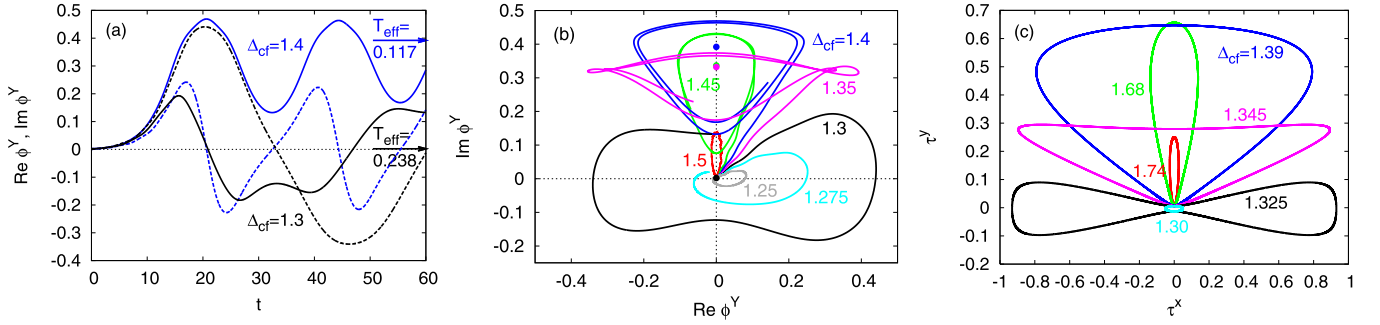
FIG. 2. [(a), (b)] Evolution of the OP after a quench from $\Delta_{cf} = 1.75$, $T = 0.2$ to the indicated values of Δ_{cf}. In panel (a), we plot the real (dashed lines) and imaginary (solid lines) part of $\phi^Y(t)$, and in panel (b) the trajectory of the OP in the complex plane. Arrows in panel (a) and colored dots in panel (b) indicate the values reached after thermalization. Panel (c) illustrates the MF dynamics for a quench from $\Delta_{cf} = 2.0$, $T = 0.3$ to the indicated values of Δ_{cf}. $\tau_Y^x \approx \sqrt{2}\mathrm{Re}\phi^Y$ and $\tau_Y^y \approx \sqrt{2}\mathrm{Im}\phi^Y$. In MF, the dynamical transition occurs at $\Delta_{cf} \approx 1.33$, whereas it happens at $\Delta_{cf} \approx 1.323$ in DMFT.

same panel, we also indicate by colored dots the values of the OPs reached after thermalization. For $1.35 \leqslant \Delta_{cf} < 1.5$, we clearly see a quench-induced symmetry breaking, with an OP that rotates around the thermal value reached in the long-time limit in an anticlockwise fashion. Between $\Delta_{cf} = 1.35$ and 1.3, a *dynamical phase transition* [38–45] (qualitative change in the evolution of the OP) occurs [52]. For $\Delta_{cf} \leqslant 1.3$, the thermal OP is zero, and the transient OP encircles the origin in a clockwise fashion. In contrast to the thermal OP with $\mathrm{Re}\phi^Y = 0$, this nonthermal OP reaches its largest values along the real axis. Since the excitonic order is related to magnetic dipoles and/or multipoles [37], the transient order observed here implies oscillations of magnetic dipoles and/or multipoles and thus oscillations of the local spin susceptibility.

A clear picture of the nonequilibrium evolution can be obtained from the mean-field (MF) dynamics of a strong-coupling effective model defined in the space of the four dominant half-filled states (one low-spin state $|L\rangle$ and three high-spin states $|H_X\rangle$, $|H_Y\rangle$, $|H_Z\rangle$) [34,35,37]. As detailed in the SM, this model has the form

$$\hat{H}_{eff} = -h_z \sum_i \hat{\tau}_i^z - h_{seed} \sum_i \hat{\tau}_{Y,i}^y + J_s \sum_{\langle ij \rangle} \hat{\mathbf{S}}_i \cdot \hat{\mathbf{S}}_j$$
$$+ J_z \sum_{\langle ij \rangle} \hat{\tau}_i^z \hat{\tau}_j^z - J_x \sum_{\langle ij \rangle} \sum_\Gamma \hat{\tau}_{\Gamma i}^x \hat{\tau}_{\Gamma j}^x - J_y \sum_{\langle ij \rangle} \sum_\Gamma \hat{\tau}_{\Gamma i}^y \hat{\tau}_{\Gamma j}^y,$$
$$(2)$$

where $\frac{1}{2}\hat{\tau}_\Gamma^{x,y,z}$ are pseudospin-$\frac{1}{2}$ operators defined in the subspace of $|H_X\rangle$ and $|L\rangle$, $\hat{\tau}_i^z = \sum_\Gamma \hat{\tau}_{\Gamma,i}^z$, h_{seed} is the seed field, $\hat{S}$ is the spin-1 operator defined in the high-spin subspace, and h_z, $J_{x,y,z,s}$ are determined by v, v', U, J, I, and Δ_{cf}. The low-spin state $|L\rangle$ yields $\tau_\Gamma^z = -1$ and zero expectation values for the other $\hat{\tau}$ and $\hat{S}$, while the OP ϕ^Γ corresponds to $\langle \hat{\tau}_\Gamma^x + i\hat{\tau}_\Gamma^y \rangle$. Figure 2(c) shows the MF dynamics of the effective model after quenches from a low-spin state above the maximum T_c. The main difference to the DMFT results is the absence of a gradually shrinking contour, which is attributed to the lack of thermalization. Still, the MF results yield a qualitatively similar dynamics, including the dynamical phase transition. As shown in the SM, $\tau_X^{x,y}$, $\tau_Z^{x,y}$, and $S^{x,y,z}$ stay zero with the occupations of $|H_{X,Z}\rangle$ fixed (m). Hence,

one can focus on the dynamics of $\boldsymbol{\tau}_Y$, which is described by the XYZ model as $H'_{eff} = -h'_z \sum_i \hat{\tau}_{Y,i}^z - h_{seed} \sum_i \hat{\tau}_{Y,i}^y + 4J_z \sum_{\langle i,j \rangle} \hat{\tau}_{Y,i}^z \hat{\tau}_{Y,j}^z - J_x \sum_{\langle i,j \rangle} \hat{\tau}_{Y,i}^x \tau_{Y,j}^x - J_y \sum_{\langle i,j \rangle} \hat{\tau}_{Y,i}^y \hat{\tau}_{Y,j}^y$, where $-h'_z = -2h_z + 2z_n(4m-1)J_z$, and z_n is the number of neighboring sites. Here, the initial low-spin state corresponds to $\boldsymbol{\tau}_Y$ parallel to $(0, 0, -1)$.

The MF evolution conserves $|\boldsymbol{\tau}_Y|$, due to the conservation of the local entropy [51]. For $t > 0$, it also conserves the total energy $\mathcal{E}(\boldsymbol{\tau}_Y)$ of the effective XYZ model, whose profile is changed abruptly by the quench. Hence, $\boldsymbol{\tau}_Y$ follows a constant-energy contour on the Bloch sphere of constant $|\boldsymbol{\tau}_Y|$, which explains the MF trajectory. In Fig. 3, we plot the $\boldsymbol{\tau}_Y$ trajectories and the energy on both sides of the dynamical phase transition. In all cases, the energy minima are at $(\tau_Y^x, \tau_Y^y, \tau_Y^z) = (0, \pm A, B)$ ($A > 0$), and before the dynamical phase transition, the $\boldsymbol{\tau}_Y$ trajectories encircle one of these minima. As we approach the transition, (i) maxima in $\mathcal{E}$ emerge at $(\tau_X^x, \tau_X^y, \tau_X^z) = (\pm A, 0, B)$, since the high-spin state $[\propto (0, 0, 1)]$ becomes energetically favorable. The transition occurs when (ii) $\mathcal{E}(0, 0, |\tau_Y|) > \mathcal{E}(0, 0, -|\tau_Y|)$ switches to $\mathcal{E}(0, 0, |\tau_Y|) < \mathcal{E}(0, 0, -|\tau_Y|)$. Elements (i) and (ii) combined have a drastic effect on the accessible contours [54] and result in a switch of the pseudospin dynamics from a rotation around the τ_Y^y axis to a rotation around the τ_Y^z axis.

In the MF picture, the nonthermal excitonic order and dynamical transition result from the conservation of the local entropy of the initial LS state (constant $|\boldsymbol{\tau}_Y|$) and the quench-induced change in the energy profile on the Bloch sphere. Here, the system is *trapped* in a cold state in the sense that it remains close to a pure state (entropy trapping). The nonthermal EI before the dynamical transition is triggered by the instability of the initial LS state toward the equilibrium EI phase. This is reminiscent of the dynamical symmetry breaking from the normal state described by the BCS theory [38,44]. However, it is nontrivial that even after the dynamical transition, where a normal HS phase is expected after thermalization, a nonthermal EI still appears due to this entropy trapping. The analysis of the DMFT local density matrix in the SM shows that the nonthermal EI is indeed close to a pure state, which supports the MF picture. In DMFT, the proximity to the integrable strong coupling limit creates a thermalization bottleneck even for $U \gtrsim$ bandwidth.
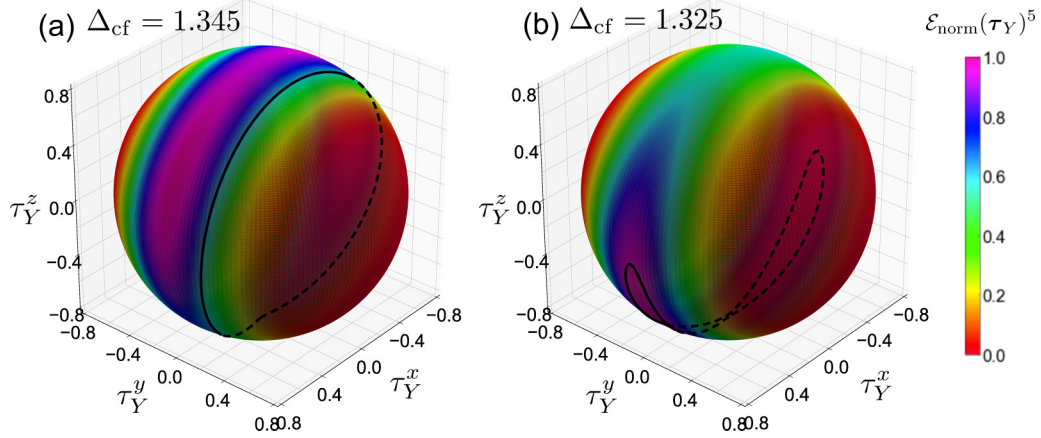
FIG. 3. MF trajectories of $\boldsymbol{\tau}_Y$ and the total energy $\mathcal{E}(\boldsymbol{\tau}_Y)$ for quenches to the indicated values of Δ_{cf} from $\Delta_{\mathrm{cf}} = 2.0$, $T = 0.3$ ($U = 6$, $J = 1$, $I = \frac{\Delta_{\mathrm{cf}}}{1.5}$, $h_{\mathrm{seed}} = \sqrt{2} \cdot 10^{-3}$). Trajectories and energies are plotted on a Bloch sphere with constant $|\boldsymbol{\tau}_Y|$ (determined by the initial state). $\mathcal{E}_{\mathrm{norm}}(\boldsymbol{\tau}_Y)$ is $\mathcal{E}(\boldsymbol{\tau}_Y)$ normalized to the range $[0,1]$ ($\mathcal{E}_{\mathrm{norm}}^5$ is plotted for better contrast).

The nonthermal nature of the EI after the quench to $\Delta_{\mathrm{cf}} = 1.3$ is also evident in the nonequilibrium spectral function $A_{a=1,\sigma}(t, \omega) = -\frac{1}{\pi} \mathrm{Im} \int_t^{t_{\max}} dt' e^{i\omega(t-t')} G_{a,\sigma}^R(t, t')$. In Figs. 4(a) and 4(c), we show the DMFT results for quenches from $\Delta_{\mathrm{cf}} = 1.75$, $T = 0.2$ to $\Delta_{\mathrm{cf}} = 1.4$ and 1.3. The gray curve shows the initial equilibrium spectrum, and the red curve indicates the nonequilibrium result for $t = 0_+$. As can be seen in Fig. 4(b), the spectrum after the quench to $\Delta_{\mathrm{cf}} = 1.4$ resembles the normal-phase equilibrium spectrum for $T \approx 0.083$, demonstrating the entropy cooling effect. As time increases, we observe the opening of the excitonic gap and oscillations of the nonequilibrium spectrum around the thermalized spectrum for $T_{\mathrm{eff}} = 0.117$. After the quench to $\Delta_{\mathrm{cf}} = 1.3$, the spectrum is very different from a cold high-spin spectrum [see Fig. 4(d)] and rather resembles the low-spin

result shown in Fig. 4(b), consistent with the aforementioned trapping. As the nonthermal OP grows, we observe oscillations around a nonthermal type of spectrum characterized by a large orbital polarization [black arrows in Fig. 4(c)] with no gap opening despite the large OP. Note that the electronic temperature extracted from the distribution function remains cold in both cases (see SM), which is direct evidence of the entropy cooling effect.

In conclusion, we showed that entropy cooling can induce symmetry breaking to an EI in the two-band Hubbard model, and we revealed a dynamical transition between a thermal-like and a distinctly nonthermal EI. Besides entropy cooling, entropy trapping due to approximate conservation laws plays an important role in stabilizing the nonthermal ordered states. Condensation can be triggered by crystal field or interaction quenches (induced, e.g., by nonlinear phononics [55,56]) and possibly via valence transitions. Promising systems to study these effects include $LaCoO_3$ [57,58], which exhibits a spin-state transition near $T = 100K$, and f-electron systems [59], where an ultrafast photo-induced valence transition with a huge increase in the local moment was recently reported. Similar entropy-cooling induced nonthermal orders can be expected in more general multiorbital systems. For example, due to a formal equivalence between our EI and the spin-triplet superconducting phase in the orbitally degenerate model away from half-filling [36], one can anticipate nonthermal spin-triplet superconductivity [60–63] above T_c induced by photo doping.

Our study furthermore revealed an interesting example of a dynamical phase transition [38–45] described by the nonequilibrium properties of the XYZ model.
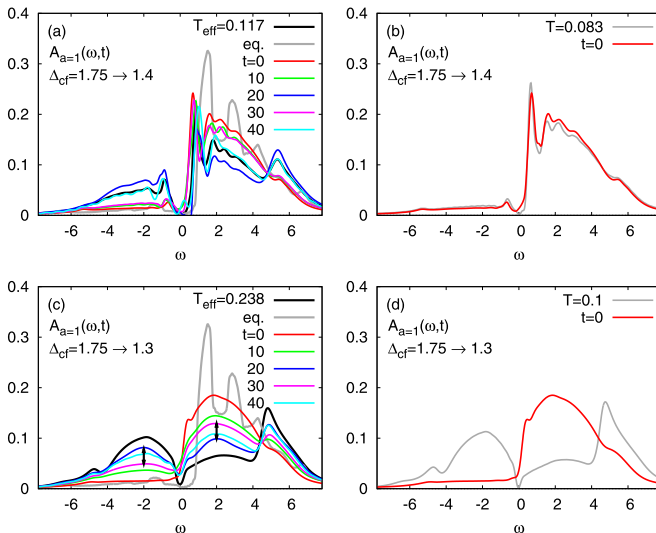

FIG. 4. Time-resolved spectral function for orbital $a = 1$ after a quench from $\Delta_{\mathrm{cf}} = 1.75$, $T = 0.2$ to $\Delta_{\mathrm{cf}} = 1.4$ (a) and 1.3 (c). The gray line represents the initial equilibrium spectrum and the black line the spectrum of the thermalized state at T_{eff}. The right panels compare the nonequilibrium spectra at $t = 0_+$ to normal phase equilibrium spectra with $\Delta_{\mathrm{cf}} = 1.4$, $T = 0.083$ (b) and $\Delta_{\mathrm{cf}} = 1.3$, $T = 0.1$ (d).

[1] D. Fausti, R. I. Tobey, N. Dean, S. Kaiser, A. Dienst, M. C. Hoffmann, S. Pyon, T. Takayama, H. Takagi, and A. Cavalleri, Science **331**, 189 (2011).

[2] S. Kaiser, C. R. Hunt, D. Nicoletti, W. Hu, I. Gierz, H. Y. Liu, M. Le Tacon, T. Loew, D. Haug, B. Keimer, and A. Cavalleri, Phys. Rev. B **89**, 184516 (2014).

[3] M. Mitrano, A. Cantaluppi, D. Nicoletti, S. Kaiser, A. Perucchi, S. Lupi, P. Di Pietro, D. Pontiroli, M. Ricco, S. R. Clark, D. Jaksch, and A. Cavalleri, Nature (London) **530**, 461 (2016).

[4] M. Buzzi, D. Nicoletti, M. Fechner, N. Tancogne-Dejean, M.A. Sentef, A. Georges, T. Biesner, E. Uykur, M. Dressel, A. Henderson, T. Siegrist, J.A. Schlueter, K. Miyagawa, K. Kanoda, M.-S. Nam, A. Ardavan, J. Coulthard, J. Tindall, F. Schlawin, D. Jaksch, and A. Cavalleri, Phys. Rev. X **10**, 031028 (2020).

[5] L. Stojchevska, I. Vaskivskyi, T. Mertelj, P. Kusar, D. Svetin, S. Brazovskii, and D. Mihailovic, Science **344**, 177 (2014).

[6] S. Mor, M. Herzog, D. Golez, P. Werner, M. Eckstein, N. Katayama, M. Nohara, H. Takagi, T. Mizokawa, C. Monney, and J. Stähler, Phys. Rev. Lett. **119**, 086401 (2017).

[7] Y. Murotani, C. Kim, H. Akiyama, L. N. Pfeiffer, K. W. West, and R. Shimano, Phys. Rev. Lett. **123**, 197401 (2019).

[8] S. J. Denny, S. R. Clark, Y. Laplace, A. Cavalleri, and D. Jaksch, Phys. Rev. Lett. **114**, 137001 (2015).

[9] M. A. Sentef, A. F. Kemper, A. Georges, and C. Kollath, Phys. Rev. B **93**, 144506 (2016).

[10] J.-i. Okamoto, A. Cavalleri, and L. Mathey, Phys. Rev. Lett. **117**, 227001 (2016).

[11] D. M. Kennes, E. Y. Wilner, D. R. Reichman, and A. J. Millis, Nat. Phys. **13**, 479 (2017).

[12] G. Mazza and A. Georges, Phys. Rev. B **96**, 064515 (2017).

[13] P. Werner, H. U. R. Strand, S. Hoshino, Y. Murakami, and M. Eckstein, Phys. Rev. B **97**, 165119 (2018).

[14] A. Nava, C. Giannetti, A. Georges, E. Tosatti, and M. Fabrizio, Nat. Phys. **14**, 154 (2018).

[15] T. Kaneko, T. Shirakawa, S. Sorella, and S. Yunoki, Phys. Rev. Lett. **122**, 077002 (2019).

[16] P. Werner, J. Li, D. Golez, and M. Eckstein, Phys. Rev. B **100**, 155130 (2019).

[17] D. M. Kennes, M. Claassen, M. A. Sentef, and C. Karrasch, Phys. Rev. B **100**, 075115 (2019).

[18] J. Tindall, B. Buca, J. R. Coulthard, and D. Jaksch, Phys. Rev. Lett. **123**, 030603 (2019).

[19] Y. Murakami, D. Golez, M. Eckstein, and P. Werner, Phys. Rev. Lett. **119**, 247601 (2017).

[20] T. Tanabe, K. Sugimoto, and Y. Ohta, Phys. Rev. B **98**, 235127 (2018).

[21] Y. Tanaka, M. Daira, and K. Yonemitsu, Phys. Rev. B **97**, 115105 (2018).

[22] E. Perfetto, D. Sangalli, A. Marini, and G. Stefanucci, Phys. Rev. Materials **3**, 124601 (2019).

[23] Y. Murakami, M. Schüler, S. Takayoshi, and P. Werner, Phys. Rev. B **101**, 035203 (2020).

[24] A. Ono and S. Ishihara, Phys. Rev. Lett. **119**, 207202 (2017).

[25] P. Werner, M. Eckstein, M. Müller, and G. Refael, Nat. Commun. **10**, 5556 (2019).

[26] J.-S. Bernier, C. Kollath, A. Georges, L. De Leo, F. Gerbier, C. Salomon, and M. Köhl, Phys. Rev. A **79**, 061601(R) (2009).

[27] M. Fabrizio, Phys. Rev. Lett. **120**, 220601 (2018).

[28] A. Mazurenko, C. S. Chiu, G. Ji, M. F. Parsons, M. Kanasz-Nagy, R. Schmidt, F. Grusdt, E. Demler, D. Greif, and M. Greiner, Nature (London) **545**, 462 (2017).

[29] C. S. Chiu, G. Ji, A. Mazurenko, D. Greif, and M. Greiner, Phys. Rev. Lett. **120**, 243201 (2018).

[30] M. Moeckel and S. Kehrein, Phys. Rev. Lett. **100**, 175702 (2008).

[31] P. Werner, N. Tsuji, and M. Eckstein, Phys. Rev. B **86**, 205101 (2012).

[32] P. Werner and A. J. Millis, Phys. Rev. Lett. **99**, 126405 (2007).

[33] T. Kaneko, K. Seki, and Y. Ohta, Phys. Rev. B **85**, 165135 (2012).

[34] J. Kunes and P. Augustinsky, Phys. Rev. B **89**, 115134 (2014).

[35] J. Kunes, J. Phys.: Condens. Matter **27**, 333201 (2015).

[36] S. Hoshino and P. Werner, Phys. Rev. B **93**, 155161 (2016).

[37] J. Nasu, T. Watanabe, M. Naka, and S. Ishihara, Phys. Rev. B **93**, 205136 (2016).

[38] R. A. Barankov, L. S. Levitov, and B. Z. Spivak, Phys. Rev. Lett. **93**, 160401 (2004).

[39] R. A. Barankov and L. S. Levitov, Phys. Rev. Lett. **96**, 230403 (2006).

[40] E. A. Yuzbashyan and M. Dzero, Phys. Rev. Lett. **96**, 230404 (2006).

[41] M. Eckstein, M. Kollar, and P. Werner, Phys. Rev. Lett. **103**, 056403 (2009).

[42] M. Schiro and M. Fabrizio, Phys. Rev. Lett. **105**, 076401 (2010).

[43] N. Tsuji, M. Eckstein, and P. Werner, Phys. Rev. Lett. **110**, 136404 (2013).

[44] N. Tsuji and P. Werner, Phys. Rev. B **88**, 165115 (2013).

[45] B. Zunkovic, M. Heyl, M. Knap, and A. Silva, Phys. Rev. Lett. **120**, 130601 (2018).

[46] A. Georges, G. Kotliar, W. Krauth, and M. J. Rozenberg, Rev. Mod. Phys. **68**, 13 (1996).

[47] H. Aoki, N. Tsuji, M. Eckstein, M. Kollar, T. Oka, and P. Werner, Rev. Mod. Phys. **86**, 779 (2014).

[48] H. Keiter and J. Kimball, Int. J. Magnetism **1**, 233 (1971).

[49] M. Eckstein and P. Werner, Phys. Rev. B **82**, 115115 (2010).

[50] This OP is related to the spin-orbital OP $o^{\mu\lambda} = \sum_{\gamma\gamma'\sigma\sigma'} \sigma^\mu_{\gamma\gamma'} \sigma^\lambda_{\sigma\sigma'} \langle c^\dagger_{\gamma\sigma} c_{\gamma'\sigma'} \rangle$ [36], for example $\phi^Y = \frac{i}{2} o^{yy}$.

[51] See Supplemental Material at http://link.aps.org/supplemental/10.1103/PhysRevB.102.241103 for additional DMFT and mean-field results, and a derivation of the strong-coupling theory and mean-field formalism.

[52] The term "dynamical phase transition" has also been used in a different context, to describe nonanalyticities in certain time-dependent quantities in the thermodynamic limit [53]. Here we use the term in the spirit of Refs. [38–45].

[53] M. Heyl, A. Polkovnikov, and S. Kehrein, Phys. Rev. Lett. **110**, 135704 (2013).

[54] One can see that there exists an energetically allowed point at $\boldsymbol{\tau}_Y = (0, C, D)$ for $E_{\text{tot}}(0, 0, |\tau_Y|) > E_{\text{tot}}(0, 0, -|\tau_Y|)$. If $E_{\text{tot}}(0, 0, |\tau_Y|) < E_{\text{tot}}(0, 0, -|\tau_Y|)$, this point is no longer energetically allowed, while one exists at $\boldsymbol{\tau}_Y = (C, 0, D)$.

[55] M. Först, R. I. Tobey, S. Wall, H. Bromberger, V. Khanna, A. L. Cavalieri, Y.-D. Chuang, W. S. Lee, R. Moore, W. F. Schlotter, J. J. Turner, O. Krupin, M. Trigo, H. Zheng, J. F. Mitchell, S. S. Dhesi, J. P. Hill, and A. Cavalleri, Phys. Rev. B **84**, 241104(R) (2011).

[56] R. Singla, G. Cotugno, S. Kaiser, M. Först, M. Mitrano, H. Y. Liu, A. Cartella, C. Manzoni, H. Okamoto, T. Hasegawa, S. R. Clark, D. Jaksch, and A. Cavalleri, Phys. Rev. Lett. **115**, 187401 (2015).

[57] P. Augustinsky, V. Krapek, and J. Kunes, Phys. Rev. Lett. **110**, 267204 (2013).

[58] M. Izquierdo, M. Karolak, D. Prabhakaran, A. T. Boothroyd, A. O. Scherz, A. Lichtenstein, and S. L. Molodtsov, Commun. Phys. **2**, 8 (2019).

[59] J. R. L. Mardegan, S. Zerdane, G. Mancini, V. Esposito, J. Rouxel, R. Mankowsky, C. Svetina, N. Gurung, S. Parchenko, M. Porer, B. Burganov, Y. Deng, P. Beaud, G. Ingold, B.

Pedrini, C. Arrell, C. Erny, A. Dax, H. Lemke, M. Decker, N. Ortiz, C. Milne, G. Smolentsev, L. Maurel, S. L. Johnson, A. Mitsuda, H. Wada, Y. Yokoyama, H. Wadati, and U. Staub, arXiv:2002.12214.

[60] J. Spalek, Phys. Rev. B **63**, 104513 (2001).

[61] J. E. Han, Phys. Rev. B **70**, 054513 (2004).

[62] M. Zegrodnik, J. Spalek, and J. Bünemann, New J. Phys. **15**, 073050 (2013).

[63] S. Hoshino and P. Werner, Phys. Rev. Lett. **115**, 247001 (2015).

[64] M. Schüler, D. Golež, Y. Murakami, N. Bittner, A. Hermann, H. U. Strand, P. Werner, and M. Eckstein, Comput. Phys. Commun. **257**, 107484 (2020).